Research article

Victor Lebedev*, Stefan Hartwig and Thomas Middelmann

Fast and robust optically pumped cesium magnetometer

https://doi.org/10.1515/aot-2020-0024
Received May 31, 2020; accepted July 28, 2020; published online October 19, 2020

Abstract: We present a fast and robust optically pumped magnetometer that is based on a feedback-controlled spin ensemble of cesium atoms in spin-polarized vapor. The table-top system is intended for operation in unshielded environment, and its design allows conversion into a handheld sensor head. Under strongly disturbed environmental conditions in the laboratory, the sensor exhibits a speed of more than 56 kHz, while having a slew rate of 39 mT/s and a full dynamic range of 10 – 120 μT. Under these conditions a sensitivity of 33 pT/$\sqrt{\text{Hz}}$ is reached. By reducing the speed to 3.6 kHz the sensitivity can be improved to 6 pT/$\sqrt{\text{Hz}}$, which is close to the shot noise limit. We describe the sensor design and its optimization and demonstrate the performance of the sensor under conditions appropriate for magnetic susceptometry measurements.

Keywords: high speed; optically detected magnetic resonance; optically pumped magnetometer; phase feedback; unshielded operation.

1 Introduction

Optically pumped atomic magnetometers (OPMs) represent a class of quantum sensors that – under suitable design optimization – can be applied to measure the magnetic field and its gradients in a broad variety of applications [1]. Most of these applications rely on operation of the OPM under magnetically silent conditions, provided by extensive magnetic shielding and ambient field compensation, for both applied biomagnetic studies [2–5] and fundamental physics research [6, 7].

Even a yet broader range of magnetometric applications would readily profit from robust sensors which are small, lightweight, and equipped with compact control and DAQ electronics. Among those are the nonlinear magnetic relaxometry [8] and susceptometry [9], conductivity testing [10], magnetic resonance imaging (MRI) [11], observation of stimulated brain response [12], or spaceborne field mapping [13]. For all of them, promising results have been demonstrated already. Nevertheless each of those applications calls for very specific sensor design and custom experimental environment, which complicates up-scaling. For example, successful commercial OPMs for geo-prospection (from Geometrics [14], GEM Systems [15], or Scintrex [16]) did not find broader applications, and zero-field OPMs from QuSpin [17] are being evaluated only in selected modalities of magnetoencephalography [18].

A common difficulty comes from incompatibility between different field settings for field source and field sensor and anticipated short source-sensor distance in view of the cubic decay of the magnetic field. On one side, strong magnetic fields are needed for sample preparation or activation, and, on the other side, low and uniform background magnetic fields are optimal for OPM operation. For some applications, not only the magnetic components or devices within the measurement system itself may perturb the OPM sensor but also the application site environment is likely to cause OPM malfunction or failure. A good example is the noninvasive testing of rechargeable batteries [10], when an OPM-based susceptometer becomes part of a factory production line and thus has to be installed in close proximity to high-current cables, electric motors or electromagnets. At the same time high efficiency shielding cannot be provided because the battery is transported into the sensor vicinity by a massive conveyor belt. This is similar to applications in medical diagnosis, which often rely on equipment infrastructure with fringing magnetic fields, including high-load elevators or even MRI scanners, producing microtesla-scale perturbations tens of meters away.

***Corresponding author: Victor Lebedev**, Physikalisch-Technische Bundesanstalt, Abbestr. 2-12, D-10587 Berlin, Germany, e-mail: victor.lebedev@ptb.de
Stefan Hartwig and Thomas Middelmann, Physikalisch-Technische Bundesanstalt, Abbestr. 2-12, D-10587 Berlin, Germany, e-mail: stefan.hartwig@ptb.de (S. Hartwig), thomas.middelmann@ptb.de (T. Middelmann)

While OPMs feature high sensitivity under shielded conditions [19], they barely demonstrate the same performance in such harsh environments. Nevertheless atomic spin ensembles in principle can be used for field sensing in up to 0.4 T fields [20]. To bridge the gap between harsh conditions and high sensitivity and optimize the sensor towards improved resilience to perturbations, higher bandwidth and broader field range, with minimal cost to sensitivity – it is worth revisiting the operation mode and design principles of OPMs, as also pursued by other groups [21–28].

In this paper, we introduce a robust OPM-setup which is capable to operate in unshielded environment with an extraordinary bandwidth, slew rate and dynamic range – which make the sensor suitable for application in magnetic relaxometry, low field nuclear magnetic resonance (NMR), or magnetic susceptometry.

2 Robust OPM design principles

Any OPM design is principally based on the coherent precession (overdamped in case of the ground state Hanle effect sensors) of an atomic spin ensemble prepared by optical pumping [29]. The angular frequency ω_L of this Larmor precession is proportional to the instantaneous magnetic field value

$$\omega_L = \gamma_F B, \tag{1}$$

where $\gamma_F = g_F \mu_B/\hbar \approx 2\pi\, 3.5\ \mathrm{s}^{-1}/\mathrm{nT}$ is the gyromagnetic ratio (here of the free cesium atom) and B is the modulus of the magnetic field. In order to interrogate the spin evolution, changes in the optical properties of the atomic ensemble are probed by the pump light or by another light beam. To observe the spin precession effects on transmitted light, one has to ensure collective atomic spin motion: by applying a small magnetic field in the case of the Hanle (zero-field) resonance [30], or by applying a small-amplitude oscillating magnetic field, commonly referred to as *rf* field, in order to excite the MR in nonzero field [31]. The modulus of the magnetic field can be extracted, e.g., from the variation of transmitted light's intensity or its polarization angle, or alternatively from intensity variations of the atomic fluorescence. The magnetic field dependence of the probed light property can be described by the MR profile $S(\gamma_F B) = S(\omega_L)$ (using Eq. (1)), which, for fixed angular frequency ω of a weak *rf* magnetic field and homogeneous broadening characterized by the spin-relaxation rate Γ, takes form

$$S(\omega_L) = \frac{S_0}{1 - i\,\frac{\omega-\omega_L}{\Gamma}} = \frac{S_0}{\sqrt{1+\left(\frac{\omega-\omega_L}{\Gamma}\right)^2}} \exp\left(- i \arctan\left(\frac{\omega-\omega_L}{\Gamma}\right)\right). \tag{2}$$

To evaluate the sensor performance we use the following key parameters:

(1) The sensitivity ρ_B, which in practice depends on the steepness of the resonance profile discriminator. In the typical case of a Lorentzian line shape (Eq. (2)), using either the quadrature or the phase profile at the resonance as discriminator, one obtains:

$$\rho_B = \frac{1}{\gamma_F}\frac{\Gamma}{S/n_s} \tag{3}$$

thus the achievable sensitivity is proportional to Γ and to the inverse of the signal S and proportional to the noise spectral density n_s.

(2) The accessible spin precession frequency range, which defines (according to Eq. (1)) the dynamic range as well as the sensor bandwidth. Here it is worth noting that a magnetic field oscillation corresponds to a spin frequency modulation.

(3) The fidelity, which refers to a weak dependence of systematic effects on changes of the environment, i.e., the stability of the MR profile under variation of the field strength and direction, as well as environmental perturbations, and robustness of the technique of field value extraction with respect to such perturbations. This includes linearity and absence of artifacts in response to fast field changes.

Ultimately those parameters are limited by fundamental processes such as the standard quantum limit – here spin-projection noise limit [32, 33], loss of spin coherence due to spin exchange [34] and loss of spin polarization due to spin-destruction collisions [35], light shift and broadening [36, 37], and photon shot noise at the detector, which can be observed under optimized laboratory conditions. Parameters of the sensor dynamics, such as the bandwidth and the field range, are fundamentally defined by the width of the MR, i.e., relaxation rate. This dependency is direct for the simplest conventional (open-loop) sensors, which only operate in the frequency band spanned by the MR and becomes indirect for closed-loop sensors, as the one described in this work, for which it is rather important in control parameter optimization.

If no precautions are taken, the resonance profile is broadened and deformed by inhomogeneous ($\Delta B \geq \Gamma/\gamma_F$) static magnetic fields and strong ($B_{AC} \geq \Gamma/\gamma_F$) oscillating

magnetic fields, – in general, non-resonant, – which leads to uncontrollable loss of sensitivity and accuracy [38]. In urban and industrial environment the performance is additionally compromised by AC electrical and acousto-mechanical perturbations.

Homogeneous magnetic perturbations can be described as slow but large field amplitude drifts, abrupt field amplitude changes and oscillations (e.g., power line) and require high field range, high slew rate and high pull-in limit [39], respectively. Common approaches to respond to those demands are to artificially broaden the resonance profile or to introduce a feedback mechanism to trace the resonance. The former can be achieved in various ways, e.g., by excessive optical power broadening or buffer gas collision broadening. However the line broadening leads to dramatic loss in the sensitivity, in the worst case scaling quadratically with the resonance line width.

Advanced quantum control methods enable to avoid such sensitivity loss. Suitable intrinsic or external spin stabilization methods allow circumventing the negative effects of the polarization relaxation processes. A prominent example of the intrinsic spin control is the so-called SERF magnetometer, which is free of influence from spin-exchange relaxation [19, 40], with the cost for the operation field range. Thanks to the simple and yet effective working principle SERF magnetometers are available as miniaturized [41] commercial products already since 2016 [17]. A similar approach is implemented in the so-called light-narrowing technique [40, 42, 43], when by careful choice of the pump laser wavelength and intensity one can suppress spin-exchange relaxation and improve sensitivity. Those techniques nevertheless do not allow us to reach a bandwidth far beyond 1 kHz while keeping high sensitivity.

The external control methods, such as feedback-based operation modes (resonance-locked M_z, M_x [28, 31, 44–46], or self-oscillating [spin maser] [22, 31, 47] configurations), rely on active tracking of the instantaneous MR peak position and "locking" to the resonance maximum. While not being directly bandwidth-limited by the spin-relaxation mechanisms, these approaches permit virtually infinite field range and bandwidth, constrained only by the instrumental capabilities of the control electronics to detect the spin response and adjust the control signal [48]. Feedback techniques are also very attractive, since they are implemented using an independent electrical subsystem, which minimally interferes with the optical preparation of the spin ensemble. The complex subject of interrelations between the spin ensemble properties, feedback parameters and resulting sensor performance is a great matter in this paper. We propose and review the model of the feedback-based OPM below and evaluate the achievable improvement of the bandwidth and dynamic performance (pull-in limit and slew rate) of the sensor.

In principle, already the proportional-only (P) controller is able to track the resonance. However such a basic control sequence may result in a significant offset of the operation point with respect to the set-point, i.e., the desired center of the resonance. In this way P-only controlled feedback sensor will principally feature low fidelity. Therefore at least a proportional-integral (PI) controller is deployed in feedback loops of OPMs. These are similar to phase-locked loops (PLLs) in the sense that the process variable is represented by the phase of the oscillation and the control variable is the frequency. However, a circuitry proven optimal for PLLs has only a limited applicability in OPMs. If the amplitude is used as discriminator then it is shaped as the imaginary part of Eq. (2), or it is arctan-shaped if the phase is used as discriminator. Both cases represent strongly non-linear dependence, since the considered process, i.e., the response of the atomic ensemble is nonlinear.

A feedback design which does not account for such nonlinearity leads to loss in the spin control under some conditions (studied in detail below), additional and narrower than those leading to inherently possible instabilities of PIDs. Since these OPM-specific features of the feedback control constrain the field range and bandwidth of the sensor, they are in the focus of this study.

Following the standard approach of the control circuit analysis, we can write down the dynamic equations of phase-feedback sensor with PI control (see sketch in Figure 2 B).

$$\phi(t) = -\arctan\left(\Omega - K\left(\phi(t) + \frac{1}{T}\int \phi(t)dt\right)\right) \qquad (4)$$

where the $\phi(t) = \phi_\Phi(t) - \phi_0$ is the phase of the loop oscillation, with the demodulated spin phase $\phi_\Phi(t)$ and resonance center phase ϕ_0 (set-point), $\Omega = \omega - \omega_L$ is the frequency difference of driving *rf* field with respect to resonance center (in units of Γ), K is the amplification of the control loop (in units of Γ) and T is the time constant of the integrator (in units of 1/Γ).

In general nonlinear feedback loops hardly can be evaluated analytically. In our case relations of the form $\Omega(\phi)$ can be obtained by solving the cubic polynomial equation after the Laplace transform of Eq. (4). The resulting expression, in its dependence on the feedback parameters K and T, is quite complex (see Appendix A). It can be used to assess the behavior of the feedback loop qualitatively, see solid trace in Figure 1, and to calculate

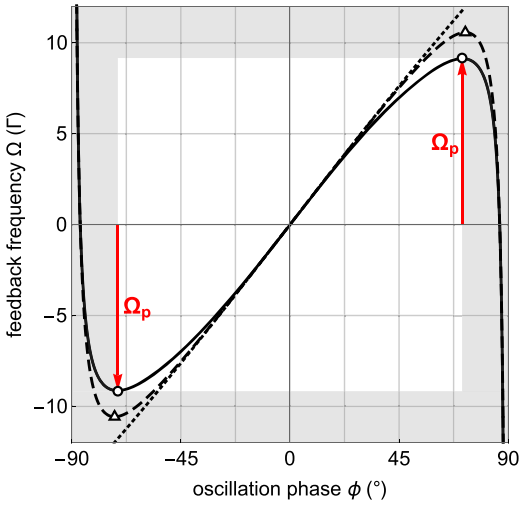

Figure 1: The detuning of the feedback frequency $\Omega(\phi)$ in units of Γ (black solid trace) with respect to the spin oscillation phase in a feedback loop described by Eq. (4) with $K = 5.43\,\Gamma$ and $T = 2\pi/(30\,\Gamma)$; quasi-linear $\phi(\omega)$ dependence (black dotted trace) represents the linear feedback loop and dashed line representing the P-only feedback with the same PI parameters. Vertical red arrows and open circles denote pull-in limits $\pm\Omega_p$ and constrain the gray area representing the inaccessible perturbation range for the feedback sensor; open triangles indicate similar limit for the P-only model.

predictions of extreme values of, e.g., the pull-in range, for fixed parameters values.

To assess the basic dynamic properties of the loop, one can assume that the argument of the arctan() in Eq. (4) does not exceed Γ, and replace the arctan() by direct proportionality, which makes the analytical evaluation of Eq. (4) simpler [39]. For a step-shaped perturbation written as $\Omega(t) = \tilde{\Omega}\,\theta(t)$ the solution:

$$\phi(t) = \frac{\tilde{\Omega}}{K-1}\exp\left(-\frac{t}{(1-1/K)T}\right) \tag{5}$$

is obtained, where θ is the Heaviside step function. From this it follows for small perturbations:

- Speed of the response of the loop is defined in the first order by the integrator time constant T and does not depend on the time constant Γ of the spin dynamics.
- For sufficiently large K and T the time of the response to an abrupt field perturbation is $T_C = (1 - 1/K)T$, which is even shorter than the delay of the integrator of T.
- For $K > 2$, the system evolves towards the unperturbed state $\phi = 0$, as if the amplitude of perturbation was $\frac{\tilde{\Omega}}{K-1} < \tilde{\Omega}$, hence the sweep time for compensation of the perturbation is reduced.

However for large perturbations, the linear approximation is not valid anymore. In the ideal case of a closed linear feedback loop the frequency range of the response is low-pass filtered with the pull-in limit as $\Omega_p \propto K$ [39]. In the nonlinear physical system represented by Eq. (4), where the phase range is asymptotically limited to $\phi_0 \pm \pi/2$, the closed-loop circuit stops sweeping the frequency beyond

$$\Omega_p^{T\to 0} = 2K\cos^{-1}\left(\frac{1}{\sqrt{2K}}\right) - \sqrt{2K-1}, \tag{6}$$

indicated in Figure 1 by the empty triangles. For very large K Eq. (6) reduces to $\Omega_p \approx \pi K$. For small K, oscillations are suppressed earlier, e.g., for $K = 5.43$, as used in the experiment discussed below, $\Omega_p^{T\to 0} \approx 10.6$ and exact solution for $T = 2\pi/(30\Gamma)$ gives significantly smaller value $\Omega_p \approx 9.1$ (circles in Figure 1). When the perturbation amplitude reaches this limit the sensor stops working until the oscillation frequency are externally reset to the vicinity of the actual Larmor frequency.

The maximal slew rate $s_B = \Omega_p/T_C$ of the sensor depends on the pull-in limit and thus is also defined by the nonlinearity of the feedback loop. For the sensor configuration discussed below the MR line can become extremely broadened with $\Gamma/2\pi = 1.3{\cdot}10^3\ \mathrm{s}^{-1}$. In this case an amplification of $K = 5.43\ \Gamma = 153\ \mathrm{s}^{-1}/^\circ$ and an integrator time constant of $T = 2\pi/(30\,\Gamma) = 21\ \mu\mathrm{s}$ lead to a Larmor frequency sweep rate of $15{\cdot}10^3\ \mathrm{s}^{-1}$ in 18 µs. The latter corresponds to a field slew rate of 39 mT/s.

All aforementioned performance indicators increase with K, however along with an increase in sensor noise. Indeed, at the resonance the solution of Eq. (4) reflects an amplification of phase fluctuations to:

$$\delta\Omega = (2K-1)\delta\phi, \tag{7}$$

compared to $\delta\Omega = \delta\phi$ for open-loop operation. Thus, the increase in the pull-in limit by a factor of $\approx (2K - 1)$ compared to the open-loop value Γ/γ_F, comes with the same increase in the noise level.

To summarize, the choice of the K and T parameters is based on different logic than for the conventional PLL. While integrator time constant T (together with K) still defines the bandwidth of the sensor and its slew rate, the value of gain K is adjusted by balancing the noise performance and the slew rate, or the pull-in limit respectively.

3 Experimental setup

The spin ensemble is prepared in a cubic quartz glass cell (custom-made, Hellma AG, $15 \times 15 \times 15\ \mathrm{mm}^3$) with 30-mm long side arm, containing about 10 mg of Cs metal. The cell's side walls are optically flat and alter the degree of

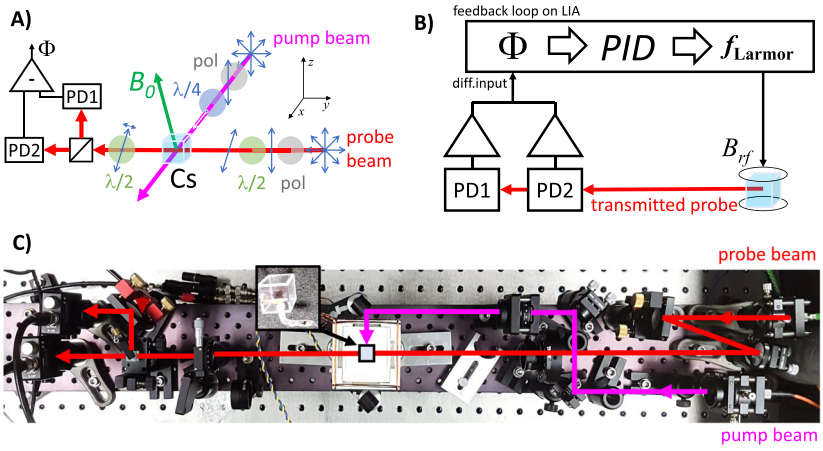

Figure 2: A Schematic arrangement of optical components: red arrows denote the probe light and the pink arrow denotes the pump light, thin blue double arrows denote the light polarization orientation (the multiarrow stars represent unpolarized light), the green arrow indicates the direction of the ambient magnetic field (offset field) B_0; green and blue disks depict waveplates ($\lambda/2$ and $\lambda/4$ respectively) and gray disks ("pol") – polarizers. The light-blue cube **Cs** represents the sensor cell and PD1 and PD2 the photodiodes which form the balanced photodetector. B) Signal processing in the setup: PD1 and PD2 denote the photodiodes of the balanced photodetector; the feedback loop is digitally implemented in the LIA (lock-in amplifier) and consists of the phase detector (Φ), whose phase output is compared to the set phase at the actual center of MR, converted to oscillation current and fed back to the vapor cell's *rf* coils with a high-bandwidth PI. C) Photograph (top view) of the assembled optical part of the setup: overlaid red arrows denote the probe light and the pink arrows denote the pump light, inset in the center shows a photograph of the used vapor cell.

transmitted light's polarization by less than 1%. Argon at 90 mbar pressure (≈ 0.1 amg) serves as buffer gas, preventing fast motion of the Cs atoms toward the cell walls. Buffer gas type and pressure are optimized in order to minimize the diffusion distance and moderately broaden the MR linewidth: both effects suppress the influence of the static and dynamic field inhomogeneity on the spin-polarized atoms. We analyzed the MR profile of the cell inside a four-layer magnetic shield (Twinleaf MS-2) and obtained a spin-relaxation rate $\Gamma = 2\pi\,50\,s^{-1}$, which is consistent with literature data on the diffusion-limited spin-relaxation rate [49] and the geometry of the cell.

The cell is enclosed in a two-compartment custom-made nonmagnetic oven. Four mutually orthogonal quartz windows allow light access into the oven in the horizontal plane through 5 mm diameter apertures. The oven design allows to warm up the cell up to 100 °C by supplying an ceramic heater in the upper compartment, above the cubic part of the cell, with AC or DC electric current. The lower, convectively heated compartment hosts the side arm of the cell, which typically is several degrees colder than the upper compartment, to avoid condensation of cesium metal drops elsewhere inside the cell. The temperature of the oven is kept at the value when the (nonspin dependent) transmission of resonant light is about 50% for the used cell. We estimate the corresponding vapor temperature to be about 55 °C and atomic density of ≈ $5{\cdot}10^{11}$ cm^{-3}. No specific measures were taken to stabilize the oven temperature apart from setting the current of the heater with 1 mA accuracy. Monitoring the resonant light transmission revealed a reproducible optical absorption and settling time in the order of minutes.

The oven is placed inside a triple of quasi-Helmholtz coils, which can generate *rf* fields of up to few μT amplitude in an arbitrary direction in the sensing volume. Coils are wound directly on the oven, thus have rectangular shape and have typical dimensions of 7 × 7 cm, which are large compared to the probed atomic cloud and thus *rf* field inhomogeneity is negligible. The oven is mounted above the solid aluminum optical breadboard using plastic posts, fixed to the breadboard with aluminum parts and nonmagnetic bolts in order to avoid systematic field inhomogeneity from standard steel or brass mechanical structures and fixtures.

3.1 Optical preparation and readout

The cesium atoms are optically pumped into the stretched spin state by a free running external-cavity diode laser (CEL002 at 894 nm from MOGLabs Pty Ltd) on the $F = 3 \rightarrow F = 4$ hyperfine component of *the buffer gas shifted and broadened* D_1 ($6S_{1/2} \rightarrow 6P_{1/2}$) transition, with power of 1 mW before entering the cell. Within the duration of a measurement (up to 1 min in the spectral sweep mode) the laser frequency varies negligibly versus the atomic transition frequency. The spin state of the atomic ensemble is probed by a second laser beam (CEL002 at 852 nm, MOGLabs) with power of about 20 μW before the cell, orthogonal to the pump beam, whose frequency is empirically set to the maximum of the spin-polarized response, which occurs about 1 GHz blue-shifted from the $F = 4 \rightarrow F = 5$ D_2 ($6S_{1/2} \rightarrow 6P_{3/2}$) transition.

The use of separate pump and probe beams enabled independent optimization of pump and probe efficiency.

Even more importantly, in the case of diffusion-limited spin motion, a high degree of spin polarization can be achieved in a narrow cylinder along the axis of the pump beam, with a radius of about the diffusion distance (≈0.3 mm for our buffer gas pressure and cell size). Both beams are delivered to the cell via optical fibers, collimated in free space and polarization-tuned by means of half- and quarter-wave plates (see Figure 2A and C). The Rayleigh length of the pump beam was about 15 mm and waist of about 0.1 mm for the pump beam, and 50 mm and 0.2 mm for the probe beam respectively. The narrow probe beam then selects a small fragment of the cylindrical-shaped pumped cloud, thus it interrogates only a small and compact volume of less than 1 mm^3. In this way, field gradients lead only to a moderate inhomogeneous broadening, corresponding to the field variation over the small interrogated volume. As a result, the sensor resilience and fidelity in general are improved.

The configuration and orientation of the waveplates are kept variable, as OPMs of the studied design feature a pronounced directional sensitivity [50], and the optimal light-polarization orientations of pump and probe beams are chosen according to the expected magnetic field direction. In the measurements presented here, the ambient field direction was close to vertical (*z*-direction) under an inclination angle $\phi \approx 20^{\circ}$, therefore the pump beam was circularly polarized and the probe beam was linearly polarized under 45° to the pump direction. This geometry is suboptimal with respect to the achieving maximal sensitivity because of high angle between pumping light polarization and ambient field. We intentionally keep this configuration, given that under strong external field perturbation not only total field modulus, but also its direction changes dynamically. Moreover, reorientation of the offset field could raise the question of partial or complete compensation of the ambient field, which demands for the large coil systems supplied with ampere-scale currents by very low noise (10^{-7} scale or better) sources. In experiments reported below, strong field perturbation is produced by – ideally zero – fringing field of the self-compensating coil, described in the next subsection. In practice its strength and direction strongly depend on the exact mechanical and thermal conditions at the instance of the measurement and affect the offset field of the sensor greatly.

While passing through the cell, the probe beam changes its polarization angle due to linear birefringence in the spin-polarized ensemble. The changes in the polarization angle are measured by a polarimeter, consisting of a polarizing beamsplitter cube and a pair of balanced photodiodes (Thorlabs DET36A), protected from room light by interference filters. An extra half-wave plate in front of the beamsplitter is used to fine-balance the differential signal.

To ensure that only the signal from the beam overlap volume contributes to the sensor response and not from other parts of the cell irradiated by the probe beam, probe laser power was set to low enough value. Therefore in absence of the pump beam no resonance signal was observed (less than 1% of the of the resonance profile amplitude in presence of the pump).

3.2 Electrical circuit and feedback loop

The output signals of the two photodiodes are separately amplified by transimpedance amplifiers (FEMTO DLPCA-200, set to 10^6 or 10^7 V/A amplification at up to 400 kHz bandwidth) and fed to the differential input of a digital lock-in amplifier (LIA, Zurich Instruments HF2LI), see Figure 2B. The photoamplifier bandwidth imposes technical upper limit on the maximal detectable Larmor frequency, and thus the field at the level of 120 μT. The feedback loop is configured using the LIA's built-in digital tool "Phase-locked loop" (PLL), with PI parameters adjusted according to the theoretical considerations above, and setting up the oscillator for technically unlimited range of the frequency excursion. The PI parameters are chosen based on the typical MR linewidth of up to $\Gamma/\pi = 1.3{\cdot}10^3$ $s^{-1}$and a carrier frequency of $\approx 1200{\cdot}10^3$ s^{-1}, corresponding to the Larmor frequency of Cs atoms in the Earth magnetic field. The set-point phase is chosen by an independent scan of the *rf* frequency over the MR prior to closing the loop (Figure 3, bottom). The feedback loop is generating a correction to the oscillator frequency, which is continuously supplied to the *rf* coils around the vapor cell. The amplitude of the *rf* magnetic field is as well chosen by a preliminary scan, such that it maximizes the MR amplitude. Since the phase of the spin precession is used to close the feedback loop, *rf* power broadening does not change the performance of the magnetometer up to the second order. Thus, quite significant changes of the MR width are tolerable, e.g., due to a changing resonance width and the resulting change in *rf* power broadening. Hence the use of phase discriminator contributes to sensor resilience.

The feedback loop frequency is continuously recorded within the LIA at a rate of 115 kS/s and is converted to the magnetic field units offline. We note that we used digital notch filters based on the instantaneous mean field values to suppress the prominent *ripple* component in all our data.

In order to test the performance of the sensor, we employed a set of coils used in a former series of

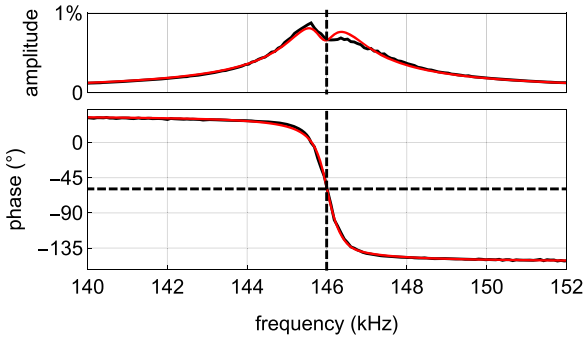

Figure 3: Spectra of magnetic resonance amplitude (top) and phase (bottom) in optically pumped atomic magnetometers (OPMs) cell, obtained by demodulating the cells transmission during the slow scan of the *rf* frequency. Black trace: experimental data, red solid lines: *rf* power–saturated model ([51]) fit of the data, vertical dashed lines: resonance position, horizontal dashed line: resonance phase, extracted from the fit of the phase curve.

experiments on magnetic particle imaging [25] for magnetization of magnetic nanoparticles, referred to as "magnetization coils" further on in the text. The choice of those coils is motivated by the ongoing research in MNP magnetorelaxometry and NMR relaxometry in our group. We used the 5 A low-noise current source (HP E3631A) to supply current to those coils. These self-shielding coil system then produces magnetic fields of up to 10 mT, typical for magnetic nanoparticle investigations, and the sensor was placed in about 8 cm from the point of the strongest field. Coils' fringing fields at the sensor position in the close vicinity are kept at a level of 10^{-3} or below, i.e., corresponding to a field variation of up to 10 µT. Fringing gradients at the sensor position are up to 1 µT/cm. Dedicated additional electrical circuit is used to enhance the rate of switching the coils' current off. As a result, complete (down to the noise level of the open circuit) switching of the field of the magnetization coils can be performed in less than 10 ms, making them a suitable benchmarking tool for the presented sensor.

4 Results and discussion

To assess the performance of the sensor below, we consider the intrinsic sensitivity ρ_B, the slew rate s_B and overall robustness of the sensor.

4.1 Intrinsic sensitivity

In order to estimate the intrinsic sensitivity of the sensor, we recorded a spectrum of the MR under unperturbed conditions in open-loop mode, demodulating amplitude and phase of the MR while scanning the *rf* frequency (Figure 3). To fit the demodulated data we use a refinement of Eq. (2), as described, e.g., in [51], to account for saturation from the *rf* magnetic field. Since the magnetometer is operated in the phase-locked mode, we extract the standard deviation of the residuals from the phase fit and divide it by the square root of the sampling rate, to obtain an estimation of the intrinsic phase noise spectral density of $n_s^\phi = 5 \cdot 10^{-3}°/\sqrt{\text{Hz}}$. As characteristic phase signal one considers $S = 1$ rad $\approx 57°$, which, divided by the phase noise spectral density, gives a signal-to-noise ratio of 12,000 in a 1 Hz bandwidth. According to Eq. (3) and with $\Gamma/2\pi = 257$ Hz, this results in an intrinsic magnetic field sensitivity $\rho_B = 6\,\text{pT}/\sqrt{\text{Hz}}$, near the shot noise limit. Latter is calculated based on the measured values of DC components of photocurrent in both arms of the balanced photodetector. Although not critical for the phase-locked operation, it is worth mentioning that we observe a significant asymmetry of the amplitude profile in all spectral scans (Figure 3, top), which we attribute to contributions of Zeeman transitions at adjacent hyperfine ground state. Due to the large broadening of the optical spectral lines, population in other level of the hyperfine manifold of the cesium ground state can be readily pumped and detected. To account for this, we have extended the fit model by introducing a weighted sum of the contributions from respective transitions to the steady state spin polarization. Within the frequency range of interest the difference of Landé factors g_F (0.32%) leads to a difference of Larmor frequencies of up to $2\pi\,500\ \text{s}^{-1}$, which is comparable to the broadening of the MR profile due to field gradients or spin relaxation. The observed asymmetry in the spectral amplitude profile can be explained by a 5% contribution of transitions to the $F = 3$ level. However, the phase profile (Figure 3, bottom), to which the magnetometer is locked to, is very modestly affected by this asymmetry.

To confirm the high-sensitivity limit in closed-loop operation, we optimized the PI parameters to achieve a minimal possible noise floor, while keeping the bandwidth as high as possible. A feedback loop bandwidth of 3.6 kHz turned out to be maximal without noise floor increase. We note here that this bandwidth is much higher than value expected based on the open-loop bandwidth (see Table 1). The corresponding noise spectrum, recorded under ambient lab conditions is plotted as the blue trace in Figure 4. It is dominated by a number of instabilities and unharmonic perturbations. The low frequency part from DC to 100 Hz is subject to $1/f$-noise. Also mechanical and acoustical noise is partially picked up due to imperfect

Table 1: Parameters of the two used optically pumped atomic magnetometers (OPMs) configurations: feedback gain K, integrator time constant T, time constant T_C of the closed-loop operation, pull-in limit Ω_p, slew rate s_B, sensitivity ρ_B, set bandwidth $R_C = 1/T_C$ and experimentally extracted field change rates R_{exp}.

Loop parameter units	K Hz/°	T µs	T_C µs	Ω_p $10^3 s^{-1}$	s_B mT/s	ρ_B $pT/\sqrt{Hz}$	R_C kHz	R_{exp} kHz
high bandwidth	153	21	18	15	39	33	56	>100
high sensitivity	38	1100	290	0.6	0.1	6	3.6	

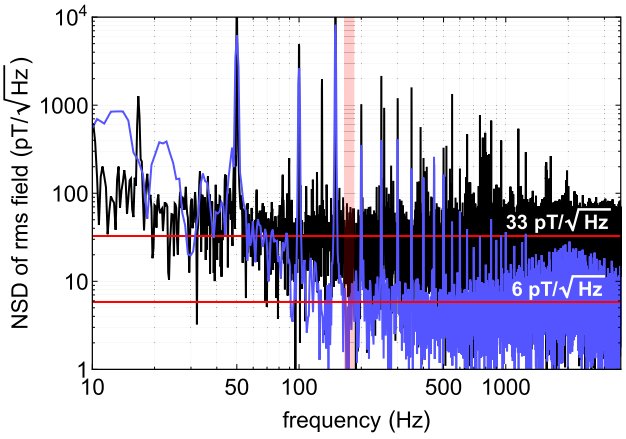

Figure 4: Spectra of the measured magnetic field noise obtained in closed-loop operation of the optically pumped atomic magnetometers (OPMs), for a feedback bandwidth of 3.6 kHz (blue trace) and 56 kHz (black trace). The vertical red-shaded area indicates the spectral range used for noise estimation of the noise levels (horizontal red lines). Note decaying high-frequency shoulders, reflecting the bandwidth limits of the sensor.

mechanical stabilization of the optical fibers and discrete optical elements of the setup. Most prominent perturbations are represented by power line noise (50 Hz) and its higher harmonics. These disturbances had indeed magnetic origin, as we were able to suppress those by four layers mu-metal Twinleaf shield. In the gaps between the power line harmonics, the noise level drops to 6 pT/$\sqrt{\text{Hz}}$, as expected from the open-loop measurements.

4.2 Large amplitude perturbations

In order to achieve maximal dynamic performance, we reconfigure the feedback loop for maximum bandwidth before the feedback loop gets unstable. Maximal nominal bandwidth of the PLL module of the HF2LI lock-in amplifier is 50 kHz under optimal PLL settings, limited by the integrator gain (or time constant for set proportional gain). Further tuning of the proportional gain K and time constant T, we achieved 56 kHz bandwidth at –3 dB level of the Bode plot of the loop's transfer function. Respective PI parameters are given in Table 1 for "high bandwidth" mode. Compared to the sensitivity optimized settings, the noise floor is now elevated in the flat part of the spectrum by half an order of magnitude (black trace in Figure 4), to about 30 pT/$\sqrt{\text{Hz}}$.

As above, the most prominent continuous perturbations are represented by power line noise and its higher harmonics. The increase of the white noise level by a factor of 5.5 is close to the expected increase of 5.8 according to Eq. (7). Those values agree within their uncertainty, which arises mainly from the ambiguity in filtering of the power line harmonics when assessing the broadband noise floor. In the low frequency range below 30 Hz the noise floor even shows some decrease, which we explain by imperfect tracking of perturbations at lower bandwidth settings of the feedback loop.

To demonstrate the bandwidth of the sensor in practice, and to confirm the absence of overshoots in the step response, we have recorded a sequence of fast field changes, using coils with 5 µs response time. We started with a comparatively small step value of 1.5 µT. In Figure 5A the recorded magnetic field (filled and open circles) together with its exponential fits (red solid lines) are compared with the slope of the coil current (blue line),

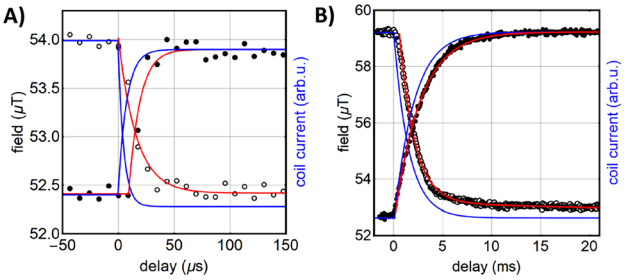

Figure 5: Time series of the sensor response to the step perturbation: A) 1.5 µT steps, B) 6.5 µT steps. Filled and open circles represent experimental field data for up and down steps respectively; solid red traces represent exponential fist of the field data; solid blue lines represent current in the coils, producing perturbations.

measured by a 5 MHz current sensor (Aim-TTi iProber 520). Transient process was fitted by the single exponential function $B_i(t_i) = B_0 + B_S\theta(t_i - t_0)e^{-R_{\exp}(t_i-t_0)}$, with fit parameters B_0, B_S, $R_{\exp}$ and t_0 freely varied. The extracted field change rate (speed) of the field detection $R_{\exp}$ was found to be about $63{\cdot}10^3$ s^{-1} at falling field slope and about $101{\cdot}10^3$ s^{-1} at rising slope, although the current is changing in both cases at the same rate of about $200{\cdot}10^3$ s^{-1}.

The current measurement reflects though only the field from the coil itself, while the time profile of the total field may have a different shape. Latter is due to contributions from magnetization of paramagnetic and ferromagnetic objects in the coil's (and the sensor's) vicinity, including the fields from eddy currents in conductive parts of the setup, such as the optical breadboard and other metallic mechanical parts. This, together with the active field zeroing at falling slope, may explain the observed asymmetry in the step response to falling and rising fields, since induced magnetization may feature different dynamics in magnetic polarization and relaxation of materials.

We note here that the applied field step amplitude (1.5 μT) is higher than the pull-in limit (700 nT), and maximal slew rate of applied field is about 300 mT/s, much higher than the predicted limit of 39 mT/s. Thus short-time instability of the sensor may occur during the fastest phase of the field switching, resulting in imperfect field tracking.

To assess the overall robustness under stronger fields, we analyze the slew rate kHz of the response of the sensor to fast field steps with high amplitude. We recorded field steps of about 6.5 μT in the high-bandwidth configuration (Figure 5B), using the "magnetization coils" described above. The used coil and current source limited the applied field's slew rate to about 3 mT/s, well below the $s_B = 39$ mT/s predicted for the sensor. However we remind the reader that this coil set produces as well the field gradients at the sensor position, which dynamically alter the MR line width. For reference, typical peak slew rates of the mains power line are in the order of only 0.03 – 0.3 mT/s in our lab.

The obtained difference of time constant of the coil current (1.5–2.0 ms) and the sensor-detected field ($1/R_{\exp}$ ≈2.0–2.5 ms) is as small as 0.5 ms. Thus the sensor in its fastest modality can be readily deployed for the measurement of 6.5 μT magnetic field changes in about half millisecond with 33 pT sensitivity, that confirms the slew rate of at least $s_B \approx 15$ mT/s.

The observed dynamic performance of the sensor makes it – even with reserves – suitable for operation in noisy lab environment, as well as in some industrial applications. Its properties allow operation under fields, typically produced by the high-current electrical instrumentation. Those parameters, combined in an analog to *gain-bandwidth product* demonstrate the resilience of the sensor to the external perturbations and exceed the performance of the commercially available OPMs by orders of magnitude. With its high bandwidth, the presented sensor also has clear advantage with respect to existing OPMs, and thanks to the relatively high sensitivity it outperforms Hall-probe and pick-up coil based instruments in the sub-kHz range.

5 Conclusions

We have presented a robust quantum magnetometer that is capable to operate in a strongly perturbing environment. It is realized as an optically pumped magnetometer in a variant of M_x configuration, detecting oscillating nonlinear magneto-optical rotation, and uses a feedback-controlled spin ensemble of cesium atoms to probe magnetic fields in unshielded environment. We have demonstrated the performance of the sensor under strongly perturbing conditions, when many electrical devices are operated in close proximity. The combination of a high speed of > 56 kHz, a pull-in range of 700 nT, a field range of 10–100 μT, while providing a sensitivity of 33 pT/$\sqrt{\text{Hz}}$, is to our knowledge unique for OPMs, — moreover, for magnetic field sensors in general it is also quite uncommon. In contrast to comparable air-core pick-up coils, aiming on similar applications as OPMs, which demonstrate superior sensitivity above 500 Hz [52], our sensor delivers flat response at DC and low frequencies, in this sense being the *universal* fast magnetometer.

We have described the design of our sensor and its specific optimization of the atomic spin preparation and probing, as well as the advanced external control of its dynamics. The analysis of the intrinsic sensitivity of the sensor revealed a value of 6 pT/$\sqrt{\text{Hz}}$ close to the shot noise limit, while the configuration of the feedback parameters in this case still allowed a bandwidth of 3.6 kHz.

While realized here as a table-top system, the design of our sensor enables conversion into, e.g., a handheld sensor head. The combination of high speed, high sensitivity, and high dynamic range at the same time makes it applicable for magnetic susceptibility and electrical conductivity measurements in an industrial environment. It can be employed for characterization of magnetic nanoparticle samples [8] or for quality assessment of batteries [10] for instance. Therefore we believe, the presented OPM design can serve as basis for a universal or crossover sensor for the

applications demanding precise detection of comparatively strong and quickly varying magnetic fields.

Author contribution: All the authors have accepted responsibility for the entire content of this submitted manuscript and approved submission.
Research funding: None declared.
Conflict of interest statement: The authors declare no conflicts of interest regarding this article.

Appendix A. Explicit form of $\Omega(\phi)$ relation

Physical phase-frequency relation resulting from Eq. (4) takes form:

$$\Omega(\phi) = -\tan\phi - \frac{c}{3\sqrt[3]{2}T^2} - \frac{\sqrt[3]{2}\left(T^2\tan^2\phi - 3\right)}{c},$$

$$a = 27T^4\left(\tan\phi - 2K\phi\right) + 2T^6\tan^3\phi - 9T^4\tan\phi,$$

$$b = \sqrt{a^2 - 4T^2\left(T^2\tan^2\phi - 3\right)^3},$$

$$c = \sqrt[3]{a+b}.$$

References

[1] D. Budker and D. F. J. Kimball, *Optical Magnetometry*, New York, Cambridge University Press, 2013.

[2] G. Bison, N. Castagna, A. Hofer, et al., "A room temperature 19-channel magnetic field mapping device for cardiac signals," *Appl. Phys. Lett.*, vol. 95, p. 17, 2009.

[3] S. Knappe, T. Sander, and L. Trahms, "Optically-pumped magnetometers for MEG," in *Magnetoencephalography: From Signals to Dynamic Cortical Networks*, S. Supek and C. J. Aine, Eds., Berlin, Heidelberg, Springer, 2014, pp. 993–999, isbn: 978-3-642-33045-2, https://doi.org/10.1007/978-3-642-33045-2_49.

[4] G. Lembke, S. N. Erné, H. Nowak, B. Menhorn, A. Pasquarelli, and G. Bison, "Optical multichannel room temperature magnetic field imaging system for clinical application," *Biomed. Optic Express*, vol. 5, no. 3, pp. 876–881, 2014. Available at: http://www.osapublishing.org/boe/abstract.cfm?URI=boe-5-3-876.

[5] E. Boto, N. Holmes, J. Leggett, et al., "Moving magnetoencephalography towards real-world applications with a wearable system," *Nature*, vol. 555, no. 7698, pp. 657–661, 2018, issn: 1476-4687.

[6] S. Pustelny, D. F. J Kimball, C Pankow et al., "The global network of optical magnetometers for exotic physics (GNOME): a novel scheme to search for physics beyond the standard model," *Ann. Phys.* 2013 525: 8659–9670.

[7] C. Abel, S. Afach, N. J. Ayres, et al., "Measurement of the permanent electric dipole moment of the neutron," *Phys. Rev. Lett.*, vol. 124, no. 8, 2020, Art no.081803, https://link.aps.org/doi/10.1103/PhysRevLett.124.081803.

[8] C. Johnson, N. L. Adolphi, K. L. Butler, et al., "Magnetic relaxometry with an atomic magnetometer and SQUID sensors on targeted cancer cells," J. Magn. Magn Mater., vol. 324, no. 17, pp. 2613–2619, 2012, issn: 0304-8853. Available at: http://www.sciencedirect.com/science/article/pii/S0304885312002582.

[9] S. Colombo, V. Lebedev, Z. D. Grujic, et al., "M(H) dependence and size distribution of SPIONs measured by atomic magnetometry," *Int. J. Magn. Part. Imag*, vol. 2, no. 1, 2016, Art no.1606002, issn: 2365–9033.

[10] Y. Hu, G. Z. Iwata, M. Mohammadi, et al., "Sensitive magnetometry reveals inhomogeneities in charge storage and weak transient internal currents in Li-ion cells," *Proc. Natl. Acad. Sci.*, vol. 117, no. 20, pp. 10667–10672, 2020, issn: 0027-8424, Available at: https://www.pnas.org/content/117/20/10667.full.pdf, https://www.pnas.org/content/117/20/10667.

[11] I. Savukov and T. Karaulanov, "Magnetic-resonance imaging of the human brain with an atomic magnetometer," *Appl. Phys. Lett.*, vol. 103, no. 4, 2013, Art no.043703.

[12] Y. HuG, Z. Iwata, T. Sander, et al., "Biomagnetic signals recorded during transcranial magnetic stimulation (TMS)-evoked peripheral muscular activity," 2019. Available at: https://arxiv.org/abs/1909.11451.

[13] M. H. Acuna, "Space-based magnetometers," *Rev. Sci. Instrum.*, vol. 73, no. 11, pp. 3717–3736, 2002.

[14] *G-864 Magnetometer*, 2020. Available at: https://www.geometrics.com/product/g-864-magnetometer/ [accessed: Jul.15, 2020].

[15] *GEM GSMP Potassium Magnetometer for High Precision and Accuracy*, 2020. Available at: https://www.gemsys.ca/ultra-high-sensitivity-potassium/[accessed: Jul.15, 2020].

[16] *ENVI Cs High Sensitivity Magnetometer*, 2020. Available at: https://scintrexltd.com/product/envi-cs/ [accessed: Jul.15, 2020].

[17] J. Osborne, J. Orton, O. Alem, and V. Shah, "Fully integrated standalone zero field optically pumped magnetometer for biomagnetism," in *Steep Dispersion Engineering and Opto-Atomic Precision Metrology XI*, vol. 10548, International Society for Optics and Photonics, 2018, Art no. 105481G.

[18] *QuSpin Blog*, 2020. Available at: https://quspin.com/blog/ [accessed: Jul.15, 2020].

[19] I. K. Kominis, T. W. Kornack, J. C. Allred, and M. V. Romalis, "A subfemtotesla multichannel atomic magnetometer," *Nature,* vol. 422, p. 596, 2003.

[20] A. Horsley and P. Treutlein, "Frequency-tunable microwave field detection in an atomic vapor cell," *Appl. Phys. Lett.*, vol. 108, no. 21, p. 211102, 2016.

[21] J. M. Higbie, E. Corsini, and D. Budker, "Robust, high-speed, all-optical atomic magnetometer," *Rev. Sci. Instrum.*, vol. 77, no. 11, p. 113106, 2006.

[22] J. Belfi, G. Bevilacqua, V. Biancalana, et al., "Dual channel self-oscillating optical magnetometer," vol. 26, no. 5, pp. 910–916, 2009, issn: 0740-3224.

[23] R. Jimenez-Martinez, W. Clark Griffith, S. Knappe, J. Kitching, and M. Prouty, "High-bandwidth optical magnetometer," *J. Opt. Soc. Am. B*, vol. 29.12, pp. 3398–3403, 2012. Available at: http://josab.osa.org/abstract.cfm?URI=josab-29-12-3398.

[24] P. Bevington, R. Gartman, and W. Chalupczak, "Alkali-metal spin maser for non-destructive tests," *Appl. Phys. Lett.*, vol. 115, no. 17, p. 173502, 2019.

[25] S. Colombo, V. Lebedev, A. Tonyushkin, S. Pengue, and A. Weis, "Imaging magnetic nanoparticle distributions by atomic magnetometrybased susceptometry," *IEEE Trans. Med. Imag.*, pp. 1, 2019, issn: 1558-254X, https://doi.org/10.1109/TMI.2019.2937670.

[26] H. Yang, K. Zhang, Y. Wang, and N. Zhao, "High bandwidth three-axis magnetometer based on optically polarized 85Rb under unshielded environment," *J. Phys. Appl. Phys.*, vol. 53.6, 2019, Art no.065002.

[27] N. Wilson, C. Perrella, R. Anderson, A. Luiten, P. Light, "Wide-bandwidth atomic magnetometry via instantaneous-phase retrieval," *Phys. Rev. Res.*, vol. 2, no. 1, 2020, Art no.013213. Available at: https://link.aps.org/doi/10.1103/PhysRevResearch.2.013213.

[28] C. O'Dwyer, S. J. Ingleby, I. C. Chalmers, P. F. Griffin, and E. Riis, "A feed-forward measurement scheme for periodic noise suppression in atomic magnetometry," *Rev. Sci. Instrum.*, vol. 91, no. 4, 2020, Art no.045103.

[29] W. Happer, "Optical pumping," *Rev. Mod. Phys.*, vol. 44(2), 169, 1972.

[30] J. Dupont-Roc, S. Haroche, and C. Cohen-Tannoudji, "Detection of very weak magnetic fields (10^{-9}gauss) by ^{87}Rb zero-field level crossing resonances," *Phys. Lett.*, vol. 28, pp. 638–639, 1969 Feb.

[31] L Arnold Bloom, "Principles of operation of the rubidium vapor magnetometer," *Appl. Optic.*, vol. 1, no. 1, pp. 61–68, 1962. Available at: http://ao.osa.org/abstract.cfm?URI=ao-1-1-61.

[32] M. Auzinsh, D. Budker, D. F. J. Kimball et al., "Can a quantum nondemolition measurement improve the sensitivity of an atomic magnetometer?," In *Phys. Rev. Lett.*, vol. 93, no. 17, 2004, Art no. 173002. Available at: https://link.aps.org/doi/10.1103/PhysRevLett.93.173002.

[33] W. Wasilewski, K. Jensen, H. Krauter, J. J. Renema, M. V. Balabas, E. S. Polzik, "Quantum noise limited and entanglement-assisted magnetometry," *Phys. Rev. Lett.*, vol. 104, no. 13, 2010, Art no. 133601. Available at: https://link.aps.org/doi/10.1103/PhysRevLett.104.133601.

[34] E. M. Purcell and G. B. Field, "Influence of collisions upon population of hyperfine states in hydrogen," *Astrophys. J.*, vol. 124, p. 542, https://doi.org/10.1086/146259.

[35] J. C. Allred, R. N Lyman, T. W. Kornack,and M. V Romalis, "High-Sensitivity atomic magnetometer unaffected by spin-exchange relaxation," *Phys. Rev. Lett.*, vol. 89, no. 13, 2002, Art no. 130801. Available at: http://link.aps.org/doi/10.1103/PhysRevLett.89.130801.

[36] B. S. Mathur, H. Tang, and W. Happer, "Light shifts in the alkali atoms," *Phys. Rev.*, vol. 171, no. 1, pp. 11–19, 1968. Available at: https://link.aps.org/doi/10.1103/PhysRev.171.11.

[37] T. Scholtes, V. Schultze, R. IJsselsteijn, S. Woetzel, and H.-G. Meyer, "Light-shift suppression in a miniaturized Mx optically pumped Cs magnetometer array with enhanced resonance signal using off-resonant laser pumping," *Optic Express*, vol. 20, no. 28, pp. 29217–29222, 2012. Available at: http://www.opticsexpress.org/abstract.cfm?URI=oe-20-28-29217.

[38] S. Colombo, V. Lebedev, A. Tonyushkin, et al., "Towards a mechanical MPI scanner based on atomic magnetometry," *Int. J. Magn. Part. Imag.*, vol. 3, no. 1, 2017, Art no. 1703006.

[39] F. M. Gardner. *Phaselock Techniques*, Hoboken: John Wiley & Sons, 2005.

[40] S. Appelt, A. Ben-Amar Baranga, A. R. Young, and W. Happer, "Light narrowing of rubidium magnetic-resonance lines in high-pressure optical-pumping cells," *Phys. Rev.*, vol. 59, no. 3, pp. 2078–2084, 1999. Available at: https://link.aps.org/doi/10.1103/PhysRevA.59.2078.

[41] P. D. D Schwindt, S. Knappe, V. Shah, et al., "Chip-scale atomic magnetometer," *Appl. Phys. Lett.*, vol. 85, no. v, pp. 6409–6411, 2004. Available at: http://aip.scitation.org/doi/abs/10.1063/1.1839274.

[42] V. Schultze, T. Scholtes, R. IJsselsteijn, and H.-G. Meyer, "Improving the sensitivity of optically pumped magnetometers by hyperfine repumping," *J. Opt. Soc. Am. B*, vol. 32, no. 5, pp. 730–736, 2015. Available at: http://josab.osa.org/abstract.cfm?URI=josab-32-5-730.

[43] R. Han, M. Balabas, C. Hovde, et al., "Is light narrowing possible with dense-vapor paraffin coated cells for atomic magnetometers?," *AIP Adv.*, vol. 7, no. 12, 2017, Art no. 125224.

[44] S. Groeger, G. Bison, J.-L. Schenker, R. Wynands, and A. Weis, "A high-sensitivity laser-pumped Mx magnetometer," *Eur. Phys. J. Atom. Mol. Opt. Phys.*, vol.38, no.2, pp. 239–247, 2006, issn: 14346079.

[45] E. B. Alexandrov and A. K. Vershovskiy, "Mx and Mz magnetometers," in *Optical Magnetometry*, D. Budker and D. F. J. Kimball, Eds., New-York, Cambridge University Press, 2013, pp. 60–84.

[46] D. Arnold, S. Siegel, E. Grisanti, J. Wrachtrup, and I. Gerhardt, "A rubidium Mx-magnetometer for measurements on solid state spins," *Rev. Sci. Instrum.*, vol. 88, no. 2, 2017, Art no.023103.

[47] W. Chalupczak and P. Josephs-Franks, "Alkali-metal spin maser," *Phys. Rev. Lett.*, vol. 115, no. 3, 2015, Art no.033004.

[48] E. B. Alexandrov and V. A. Bonch-Bruevich, "Optically pumped atomic magnetometers after three decades," *Opt. Eng.*, vol. 31, no. 4, pp. 711–717, 1992.

[49] A. Corney, *Atomic and Laser Spectroscopy*, Oxford: Oxford University Press, 1977.

[50] S. Colombo, V. Dolgovskiy, T. Scholtes, Z. D. Grujić, V. Lebedev, and A. Weis, "Orientational dependence of optically detected magnetic resonance signals in laser-driven atomic magnetometers," *Appl. Phys. B*, vol. 123, no. 1, pp. 35–0649, 2016, issn: 1432.

[51] G. Bison, R. Wynands, and A. Weis, "Optimization and performance of an optical cardiomagnetometer," *J. Opt. Soc. Am. B*, vol. 22.1, pp. 77–87, 2005.

[52] R. Pellicer-Guridi, M. W. Vogel, D. C. Reutens, and V. Vegh, "Towards ultimate low frequency air-core magnetometer sensitivity," *Sci. Rep.*, vol. 7, no. 1, pp. 2269–2322, 2017, issn: 2045.

Bionotes

Victor Lebedev
Physikalisch-Technische Bundesanstalt, Abbestr. 2-12, D-10587 Berlin, Germany
victor.lebedev@ptb.de

Victor Lebedev was born in St. Petersburg, Russia in 1979 and graduated with the MS degree in physics from the St. Petersburg State University in 2002. He studied physics and received the PhD degree from the University of Fribourg, Switzerland in 2011. In 2018 he joined Optical Magnetometry group at the Physikalisch-Technische Bundesanstalt, Berlin, Germany. His research interests are focused on application of atomic spin probes in quantum solids, cold, and hot gases to magneto-optical investigations of collision processes and precision measurements of magnetic fields.

Stefan Hartwig
Physikalisch-Technische Bundesanstalt, Abbestr. 2-12, D-10587 Berlin, Germany
stefan.hartwig@ptb.de

Stefan Hartwig was born in Berlin, Germany in 1968. He studied applied physics and medical engineering at the Beuth University of applied sciences, Berlin, Germany and received the Dipl.-Ing. (FH) in 1994 and the M.Eng. in 2006. In 2011 he received his PhD degree in Biomedical Engineering from Technical University Ilmenau. Since 1996 he has been a staff member of the Physikalisch-Technische Bundesanstalt (PTB), Berlin, Germany, where he has been working in the fields of biomagnetism, magnetic nanoparticles, ultra-low field NMR, and optical magnetometry

Thomas Middelmann
Physikalisch-Technische Bundesanstalt, Abbestr. 2-12, D-10587 Berlin, Germany
thomas.middelmann@ptb.de

Thomas Middelmann was born in Berlin, Germany in 1979. He studied physics at the Technical University of Berlin, Germany and the Rijksuniversiteit Groningen, Netherlands. He received the Diploma in physics in 2007 and the PhD degree from the University of Hannover, Germany, in 2013. Since 2008 he has been a staff member of the Physikalisch-Technische Bundesanstalt (PTB), Braunschweig, and later Berlin, Germany, where he has worked in the fields of quantum optics, interferometry and (bio-)magnetic measurements. Since 2019 he has been leading the “Optical Magnetometry” group at PTB in Berlin.